

Modelling droplets on superhydrophobic surfaces: equilibrium states and transitions

A. Dupuis and J.M. Yeomans

The Rudolf Peierls Centre for Theoretical Physics, University of Oxford,
1 Keble Road, Oxford OX1 3NP, UK.

November 5, 2018

Abstract

We present a lattice Boltzmann solution of the equations of motion describing the spreading of droplets on topologically patterned substrates. We apply it to model superhydrophobic behaviour on surfaces covered by an array of micron-scale posts. We find that the patterning results in a substantial increase in contact angle, from 110° to 156° . The dynamics of the transition from drops suspended on top of the posts to drops collapsed in the grooves is described.

1 Introduction

From microfluidic technology to detergent design and ink-jet printing it is vital to understand the way in which drops move across surfaces. The dynamics of the drops will be affected by any chemical or topological heterogeneities on the surface. Until recently such disorder was usually regarded as undesirable. However with the advent of microfabrication techniques it has become possible to control the chemical or topographical patterning of a substrate on micron length scales, leading to the possibility of exploring new physics and to novel applications.

A beautiful example of this, inspired by the leaves of the lotus plant, are superhydrophobic substrates. These are surfaces which are covered with posts on length scales of order microns. As a result of the topological patterning they are strongly repellent to water droplets which show contact angles up to 160° [1, 2, 3].

This should be compared to more traditional ways of increasing the contact angle, surface coatings and chemical modifications of the substrate, where it is difficult to achieve an angle of more than 120° . Superhydrophobic substrates have many potential applications, for example as materials for raincoats or windscreens. The evolutionary advantage to the lotus appears to be the easy run-off which helps to clean the leaves of the plant.

Droplets on a superhydrophobic surface can be in two states, suspended where the drop sits on top of the posts with pockets of air beneath it, or collapsed where it wets the grooves between the posts. Several authors have calculated the free energies of the suspended and collapsed states using approximations based on the Cassie-Baxter and Wenzel laws respectively [4, 5]. They have shown that both states can be thermodynamically stable with the phase boundary between them depending on the surface tension and substrate geometry. It has also been argued that the suspended drop is often observed as a metastable state as it has to cross a free energy barrier to fill the grooves. However the kinetics of the transition to the collapsed phase is not understood: it is not accessible to the equilibrium theories and it is hard to probe experimentally.

Therefore in this paper we present a numerical solution to equations which are able to describe both the static and dynamic behaviour of droplets on topologically patterned substrates. The droplet dynamics is described by the Navier-Stokes equations for a liquid-gas system. Its equilibrium behaviour corresponds to a chosen free energy functional so that appropriate thermodynamic information, such as the surface tension and the contact angle, are included in the model. We solve the equations of motion using a lattice Boltzmann algorithm. This approach has a natural length scale, for fluids such as water, of order microns where much of the exciting new physics is expected to appear. The method has already shown its capability in dealing with spreading on surfaces with chemical patterning [6].

In section 2 we summarise the algorithm and, particularly, describe the new thermodynamic and velocity boundary conditions needed to treat surfaces with topological patterning. In section 3 we present results for a substrate patterned by an array of posts and show that the patterning leads to a substantial increase in contact angle in agreement with experiments. We then explore the kinetics of the transition between the suspended and collapsed droplet states. Finally we discuss directions for future work using this approach.

2 The mesoscopic model

2.1 Equilibrium free energy

We consider a liquid-gas system of density $n(\mathbf{r})$ and volume V . The surface of the substrate is denoted by S . The equilibrium properties of the drop are described by the free energy

$$\Psi = \int_V \left(\psi_b(n) + \frac{\kappa}{2} (\partial_\alpha n)^2 \right) dV + \int_S \psi_c(n) dS. \quad (1)$$

where Einstein notation is understood for the Cartesian label α (i.e. $v_{i\alpha}u_\alpha = \sum_\alpha v_{i\alpha}u_\alpha$) and where $\psi_b(n)$ is the free energy in the bulk. We conveniently choose the double well form [7]

$$\psi_b(n) = p_c (\nu_n + 1)^2 (\nu_n^2 - 2\nu_n + 3 - 2\beta\tau_w) \quad (2)$$

where $\nu_n = (n - n_c)/n_c$, $\tau_w = (T_c - T)/T_c$ and $p_c = 1/8$, $n_c = 7/2$ and $T_c = 4/7$ are the critical pressure, density and temperature respectively and β is a constant typically equal to 0.1.

The derivative term in equation (1) models the free energy associated with density gradients at an interface. κ is related to the surface tension γ by [7]

$$\gamma = \frac{4}{3} \sqrt{2\kappa p_c} (\beta\tau_w)^{3/2} n_c. \quad (3)$$

$\psi_c(n_s) = -\phi_1 n_s$ is the Cahn surface free energy [8] which controls the wetting properties of the fluid. In particular ϕ_1 can be used to tune the contact angle.

2.2 Navier-Stokes equations

The dynamics of the droplet is described by the Navier-Stokes equations for a non-ideal gas

$$\begin{aligned} \partial_t(nu_\alpha) + \partial_\beta(nu_\alpha u_\beta) &= -\partial_\beta P_{\alpha\beta} + \nu \partial_\beta [n(\partial_\beta u_\alpha + \partial_\alpha u_\beta + \delta_{\alpha\beta} \partial_\gamma u_\gamma)] + nF_\alpha, \\ \partial_t n + \partial_\alpha(nu_\alpha) &= 0 \end{aligned} \quad (4)$$

where $\mathbf{u}(\mathbf{r})$ is the fluid velocity, ν the kinematic viscosity and \mathbf{F} a gravitational field. The pressure tensor $P_{\alpha\beta}$ is related to the free energy by [9]

$$P_{\alpha\beta} = \frac{\partial \mathcal{F}}{\partial (\partial_\alpha n)} (\partial_\beta n) - \mathcal{F} \delta_{\alpha\beta} \quad (5)$$

where $\mathcal{F} = \psi_b - \mu_b n + \kappa (\partial_\alpha n)^2 / 2$ and $\mu_b = 4p_c(1 - \beta\tau_w)/n_c$ is the bulk chemical potential.

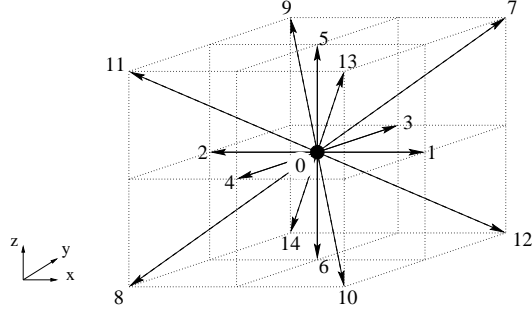


Figure 1: Topology of a $D3Q15$ lattice. The directions i are numbered and correspond to the velocity vectors \mathbf{v}_i .

2.3 The lattice Boltzmann algorithm

We solve the equations of motion (4) by using a lattice Boltzmann algorithm. This approach follows the evolution of partial distribution functions f_i on a regular, d -dimensional lattice formed of sites \mathbf{r} . The label i denotes velocity directions and runs between 0 and z . $DdQz + 1$ is a standard lattice topology classification. The $D3Q15$ lattice we use here has the following velocity vectors \mathbf{v}_i : $(0, 0, 0)$, $(\pm 1, \pm 1, \pm 1)$, $(\pm 1, 0, 0)$, $(0, \pm 1, 0)$, $(0, 0, \pm 1)$ in lattice units as shown in fig. 1.

The lattice Boltzmann dynamics are given by

$$f_i(\mathbf{r} + \Delta t \mathbf{v}_i, t + \Delta t) = f_i(\mathbf{r}, t) + \frac{1}{\tau} (f_i^{eq}(\mathbf{r}, t) - f_i(\mathbf{r}, t)) + n w_\sigma v_{i\alpha} F_\alpha \quad (6)$$

where Δt is the time step of the simulation, τ the relaxation time. σ labels velocities of different magnitude, $w_1 = 1/3$, $w_2 = 1/24$. f_i^{eq} is the equilibrium distribution function which is a function of the density $n = \sum_{i=0}^z f_i$ and the fluid velocity \mathbf{u} , defined through the relation

$$n \mathbf{u} = \sum_{i=0}^z f_i \mathbf{v}_i. \quad (7)$$

The relaxation time tunes the kinematic viscosity as

$$\nu = \frac{(\Delta \mathbf{r})^2}{\Delta t} \frac{1}{3} \left(\tau - \frac{1}{2} \right) \quad (8)$$

where $\Delta \mathbf{r}$ is the lattice spacing.

It can be shown [10] that equation (6) reproduces the Navier-Stokes equations of a non-ideal gas (4) if the local equilibrium functions are chosen as

$$\begin{aligned} f_i^{eq} &= A_\sigma + B_\sigma u_\alpha v_{i\alpha} + C_\sigma \mathbf{u}^2 + D_\sigma u_\alpha u_\beta v_{i\alpha} v_{i\beta} + G_{\sigma\alpha\beta} v_{i\alpha} v_{i\beta}, \quad i > 0, \\ f_0^{eq} &= n - \sum_{i=1}^z f_i^{eq}. \end{aligned} \quad (9)$$

A possible choice of the coefficients is [11]

$$\begin{aligned} A_\sigma &= \frac{w_\sigma}{c^2} \left(p_0 - \frac{\kappa}{2} (\partial_\alpha n)^2 - \kappa n \partial_{\alpha\alpha} n + \nu u_\alpha \partial_\alpha n \right), \\ B_\sigma &= \frac{w_\sigma n}{c^2}, \quad C_\sigma = -\frac{w_\sigma n}{2c^2}, \quad D_\sigma = \frac{3w_\sigma n}{2c^4}, \\ G_{1\gamma\gamma} &= \frac{1}{2c^4} (\kappa (\partial_\gamma n)^2 + 2\nu u_\gamma \partial_\gamma n), \quad G_{2\gamma\gamma} = 0, \\ G_{2\gamma\delta} &= \frac{1}{16c^4} (\kappa (\partial_\gamma n) (\partial_\delta n) + \nu (u_\gamma \partial_\delta n + u_\delta \partial_\gamma n)) \end{aligned} \quad (10)$$

where $c = \Delta \mathbf{r} / \Delta t$ and $p_0 = n \partial_n \psi_b - \psi_b = p_c (\nu_n + 1)^2 (3\nu_n^2 - 2\nu_n + 1 - 2\beta\tau_w)$.

2.4 Wetting boundary conditions

The major challenge in dealing with patterned substrates is to handle the boundary conditions correctly. We consider first wetting boundary conditions which control the value of the density derivative and hence the contact angle. For flat substrates a boundary condition can be established by minimising the free energy (1) [8]

$$\hat{\mathbf{s}} \cdot \nabla n = -\frac{\phi_1}{\kappa} \quad (11)$$

where $\hat{\mathbf{s}}$ is the unit vector normal to the substrate. It is possible to obtain an expression relating ϕ_1 to the contact angle θ as [7]

$$\phi_1 = 2\beta\tau_w \sqrt{2p_c \kappa} \operatorname{sign} \left(\frac{\pi}{2} - \theta \right) \sqrt{\cos \frac{\alpha}{3} \left(1 - \cos \frac{\alpha}{3} \right)} \quad (12)$$

where $\alpha = \cos^{-1}(\sin^2 \theta)$ and the function sign returns the sign of its argument.

Equation (11) is used to constrain the density derivative for sites on a flat part of the substrate. However, no such exact results are available for sites at edges or corners. We work on the principle that the wetting angle at such sites should be

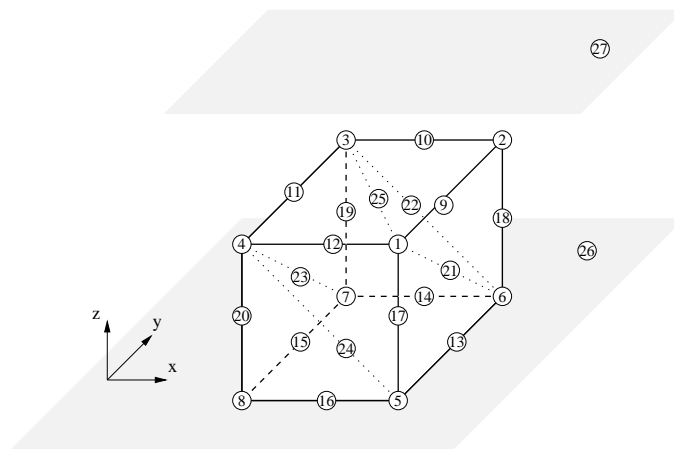


Figure 2: Sketch of a post on a substrate. Encircled numbers label sites in different topological positions. Labels 26 and 27 denote sites on the bottom ($z = z_{min}$) and the top ($z = z_{max}$) of the domain respectively.

constrained as little as possible so that, in the limit of an increasingly fine mesh, it is determined by the contact angle of the neighbouring flat surfaces.

For edges (labels 9 – 12 in fig. 2) and corners (labels 1 – 4) at the top of the post each site has 6 neighbours on the computational mesh. Therefore these sites can be treated as bulk sites.

At bottom edges where the post abuts the surface (labels 13 – 16 in fig. 2) density derivatives in the two directions normal to the surface (e.g. x and z for sites labeled 13) are calculated using

$$\partial_z n = \partial_{x/y} n = -\frac{1}{\sqrt{2}} \frac{\phi_1}{\kappa} \quad (13)$$

where the middle term constrains the density derivative in the appropriate direction x or y .

At bottom corners where the post joins the surface (labels 5 – 8 in fig. 2) density derivatives in both the x and y directions are known. Therefore these sites are treated as planar sites.

2.5 Velocity boundary conditions

We impose a no-slip boundary condition on the velocity by determining the missing fields which fulfill the no-slip condition given by equation (7) with $\mathbf{u} = 0$. This does not uniquely determine the f_i 's. For most of the cases (i.e. 1 – 20) arbitrary choices guided by symmetry are used to close the system. This is no longer possible for sites 21 – 27 where four asymmetrical choices are available. Selecting one of those solutions or using a simple algorithm which chooses one of them at random each time step leads to very comparable and symmetrical results. Hence we argue that an asymmetrical choice can be used. Possible conditions, which are used in the results reported here, are listed in appendix A.

The conservation of mass is ensured by setting a suitable rest field, f_0 , equal to the difference between the density of the missing fields and the one of the fields entering the solid after collision.

In a hydrodynamic description of wetting contact line slip must be introduced in some way. As with other phase field models slip appears naturally within the lattice Boltzmann framework. The mechanism responsible for the slip is evaporation and condensation of the fluid because of a non-equilibrium curvature of the contact line [7, 12].

3 Results

We consider the superhydrophobic behaviour of droplet spreading on a substrate patterned by square posts arranged as in fig. 3. The size of the domain is $L_x \times L_y \times L_z = 80 \times 80 \times 80$ and the height, spacing and width of posts are $h = 5$, $d = 8$ and $w = 4$ respectively. A spherical droplet of radius $R = 30$ is initially centered within the domain and just touches the post tops. The contact angle $\theta^{eq} = 110^\circ$ is set on every substrate site. The surface tension and the viscosity are tuned by choosing parameters $\kappa = 0.002$ and $\tau = 0.8$ respectively. The liquid density n_l and gas density n_g are set to $n_l = 4.128$ and $n_g = 2.913$ and the temperature $T = 0.4$.

Simulation and physical parameters can be related by choosing a length scale Δr , a time scale Δt and a mass scale Δm . A simulation parameter with dimensions $[L]^{n_1}[T]^{n_2}[M]^{n_3}$ is multiplied by $\Delta r^{n_1}\Delta t^{n_2}\Delta m^{n_3}$ to give the physical value. For example, considering a 1 mm droplet of a fluid of kinematic viscosity $\nu = 3 \cdot 10^{-5} \text{ m}^2\text{s}^{-1}$ and surface tension $1 \cdot 10^{-3} \text{ Nm}^{-1}$ leads to $\Delta r = 1.7 \cdot 10^{-5} \text{ m}$, $\Delta t = 9.3 \cdot 10^{-7} \text{ s}$, $\Delta m = 1.6 \cdot 10^{-12} \text{ kg}$. That implies $n_l = 1.4 \cdot 10^3 \text{ kgm}^{-3}$.

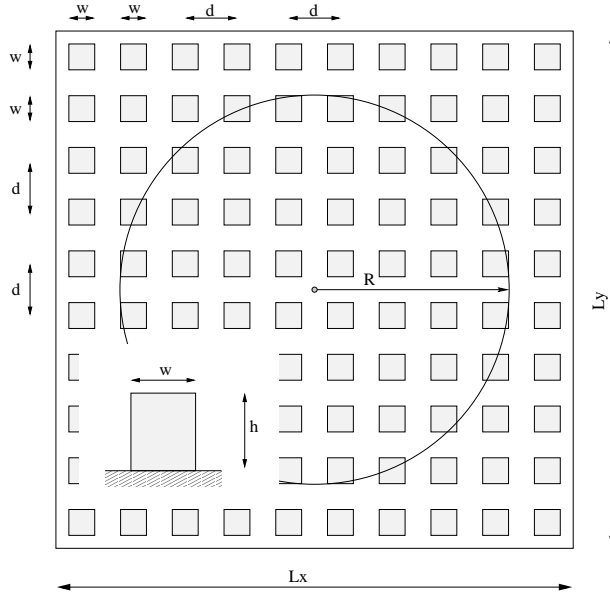


Figure 3: Plan view of the substrate. Shaded areas are posts.

However, as with all diffuse interface models the liquid-gas density difference is unphysically small and the width of the interface is too large. This must be taken into account by renormalising the time scale.

3.1 Equilibrium states

Fig. 4 shows the final state attained by the droplet for different substrates or initial conditions. For comparison fig. 4(a) shows a planar substrate. The equilibrium contact angle is $\theta^{flat} = 110^\circ = \theta^{eq}$ as expected [11]. In fig. 4(b) the substrate is patterned and the initial velocity of the drop is zero. Now the contact angle is $\theta^s = 156^\circ$, a demonstration of superhydrophobic behaviour. Fig. 4(c) reports an identical geometry but a drop with an initial impact velocity. Now the drop is able to collapse onto the substrate and the final angle is $\theta^c = 130^\circ$. These angles are compatible with the ones reported in [2].

Superhydrophobicity occurs over a wide range of d , the distance between the posts. For suspended drops of $R = 30$ and $d \gtrsim 12$ the drop resides on a single post and the contact angle is 170° . For $d \lesssim 12$ the contact angle lies between 148° and 156° with the range primarily due to the commensurability between drop radius

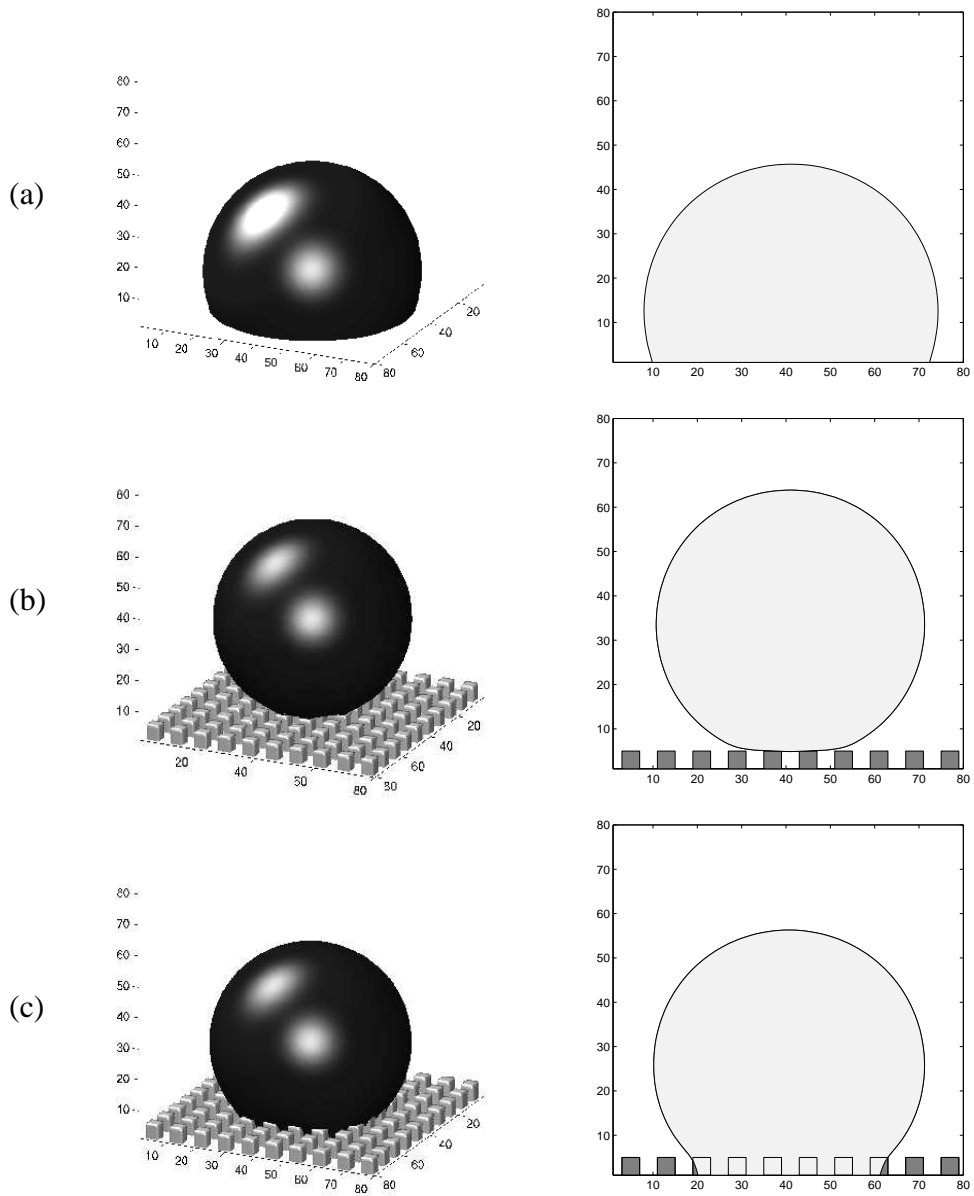


Figure 4: Final states of a spreading droplet. The right column reports vertical cuts across the centre of the drop. (a) The substrate is flat and homogeneous. (b) The substrate is decorated with posts and the initial velocity of the droplet is zero. (c) Same geometry as (b) but the droplet reaches the substrate with a velocity $u_z = -0.01$.

and post spacing.

3.2 Kinetics of the suspended to collapsed transition

We now investigate the kinetics of the transition between the suspended and collapsed droplet states. For the parameter values used in the simulations presented in fig. 4 the state with the drop suspended on the posts has a slightly higher free energy than the collapsed state. However as the drop penetrates the grooves the area of the contact between liquid and solid increases. Because the substrate is hydrophobic this creates a free energy barrier hindering the transition from the suspended to the collapsed states. Work must be provided, by an impact velocity or gravity say, to allow the transition to proceed [13, 3].

We follow the transition pathway by considering a spherical droplet of radius $R = 30$ initially centered within the domain and just touching the top of the posts. A gravitational field F_z is turned on at time $t = 70000$, and turned off at $t = 200000$. Fig. 5 shows cross sections of the drop as it undergoes the transition from the suspended to the collapsed state for $F_z = -5 \cdot 10^{-7}$. Note how the substrate interstices are filled successively from the drop centre to its edges.

The time evolution of the total free energy of the system is presented in fig. 6 for two different values of F_z . We plot Ψ_T the total free energy; the volume Ψ_v and surface Ψ_s contributions to the free energy which arise from the first and second integral in (1) respectively and the contribution from the gravitational force

$$\Psi_g = \int_V n z F_z dV. \quad (14)$$

The solid lines in fig. 6 correspond to the snapshots in fig. 5. After gravity is switched on the drop is pushed down and hence Ψ_g decreases. On the other hand Ψ_s increases as the surface is covered by liquid rather than by gas corresponding to a free energy gain for a hydrophobic surface. Ψ_v also initially increases as the interface is deformed. Once the drop touches the bottom of the interstices Ψ_v drops sharply because parts of the interface have just vanished. At the same time Ψ_s grows significantly because a part of the surface is now in contact with the liquid rather than with air. At $t = 200000$, the gravitational field is turned off. The squeezed droplet dewets to recover a spherical shape and Ψ_s decreases. The total free energy is slightly smaller in the collapsed state.

The figures show that both the surface and the volume energies increase during the transition. Hence, as the total free energy must decrease, the transition could

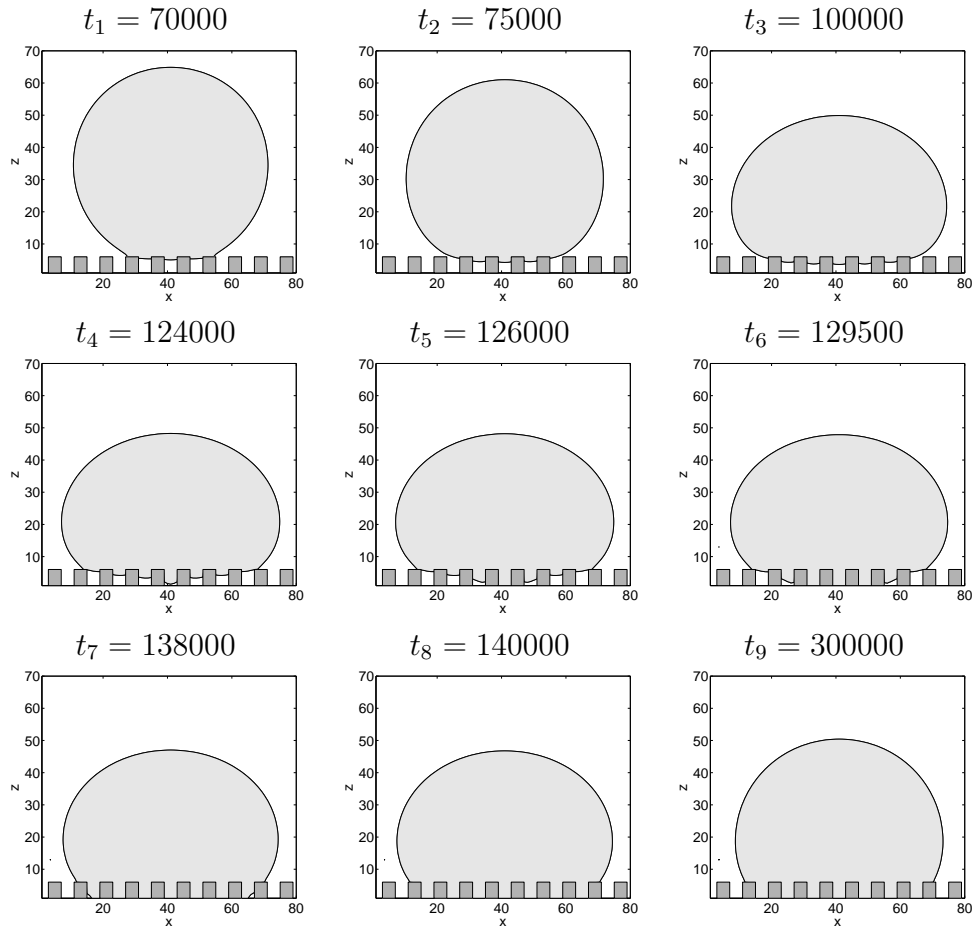


Figure 5: Transition from a suspended to a collapsed state. The gravity field $F_z = 5 \cdot 10^{-7}$. These cuts are vertical cross sections across the centre of the domain where the dark gray areas are the posts and the pale ones are liquid regions.

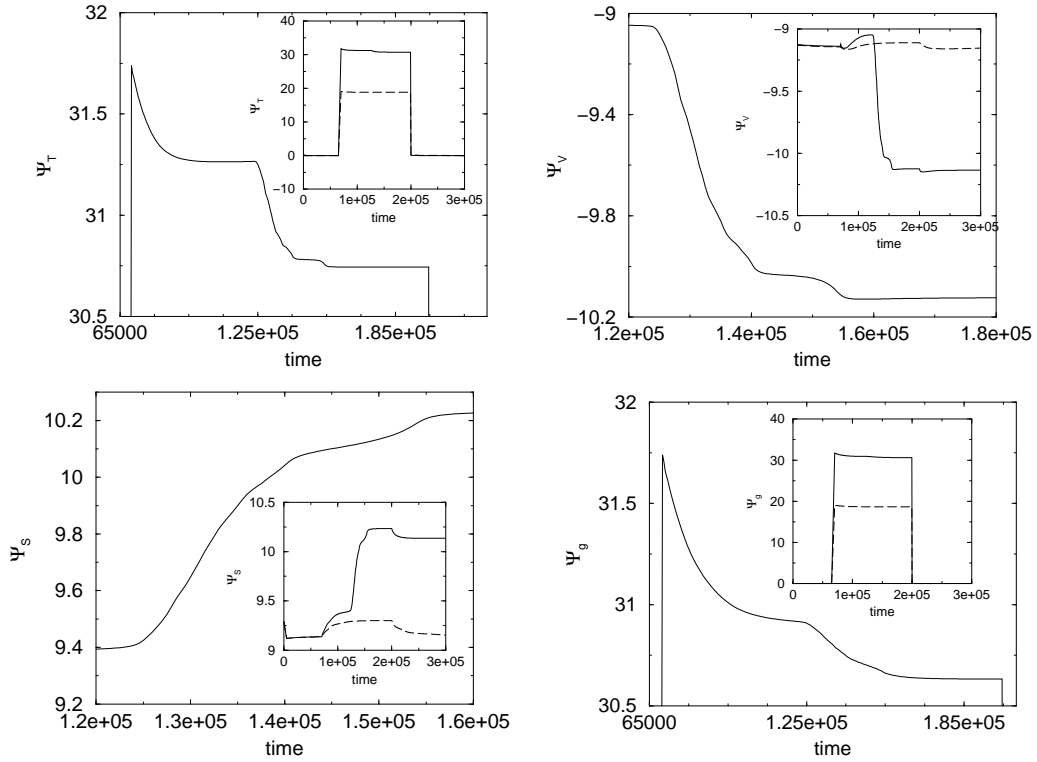


Figure 6: Evolution of the free energies of superhydrophobic drops. A body force F_z is turned on at $t = 70000$ and turned off at $t = 200000$. Solid and dashed lines corresponds to free energies when $F_z = -5 \cdot 10^{-7}$ and $F_z = -3 \cdot 10^{-7}$ respectively. The axes are in simulation units with free energy chosen to be zero at equilibrium. In each case the larger diagram highlights the free energy and time regimes where the most interesting behaviour occurs. The insets show the behaviour throughout the simulation.

not occur without the addition of a gravitational force. The decrease in the gravitational free energy offsets the increase in the surface and volume terms allowing the transition to proceed. Essentially the addition of F_z removes the barrier which the total free energy must surmount.

A lower gravitational field, $F_z = 3 \cdot 10^{-7}$, does not allow the drop to overcome the free energy barrier and it remains in the suspended state as shown by the dashed lines in fig. 6.

For example, considering again a 1 mm droplet of a fluid of kinematic viscosity $\nu = 3 \cdot 10^{-5} \text{ m}^2\text{s}^{-1}$ and surface tension $1 \cdot 10^{-3} \text{ Nm}^{-1}$, $F_z = 5 \cdot 10^{-7}$ would correspond to 9.7 ms^{-2} in physical units.

4 Conclusion

We have used a lattice Boltzmann approach to solve the equations of motion describing the dynamics of a drop on topologically patterned substrate. The approach allows us to simulate the dynamic and equilibrium properties of a drop with a given size, surface tension, contact angle and viscosity. Because interfaces appear naturally within the model it is particularly well suited to looking at the behaviour of evolving drops.

In particular we have considered a droplet positioned on an array of posts and shown that it is possible to reproduce the superhydrophobic behaviour seen in experiments. The ability of the algorithm to follow the drop kinetics has enabled us to investigate the transitions between the suspended state where the drop lies on top of the posts and the collapsed state where it fills the spaces between them. We find that the substrate interstices are filled successively starting from the drop centre.

There are many avenues open for further investigation. For example we are currently investigating how drops move across hydrophobic surfaces to compare to recent experiments. It would also be interesting to follow the spreading of drops on surfaces with topological imperfections, a problem of concern in the quality of images formed in ink-jet printing.

Acknowledgment

We thank the Oxford Supercomputing Centre for providing supercomputing resources. AD acknowledges the support of the EC IMAGE-IN project GR1D-CT-

2002-00663.

A Possible boundary conditions

We list here the boundary conditions used to define missing distribution functions, i.e. those that stream from positions outside the simulation box.

Label (see fig.2)	Conditions
1	$f_{13} = f_{14}$
2	$f_7 = f_8$
3	$f_9 = f_{10}$
4	$f_{11} = f_{12}$
5	$f_5 = f_6$ $f_{13} = (f_3 - f_4 - f_1 + f_2)/2 + f_9 + f_{14} - f_{10}$ $f_{11} = (f_1 - f_2)/2 - f_9 + f_{10} + f_{12}$ $f_7 = (-f_3 + f_4)/2 + f_8 - f_9 + f_{10}$
6	$f_5 = f_6$ $f_{13} = (f_3 - f_4)/2 - f_{11} + f_{12} + f_{14}$ $f_9 = (f_1 - f_2)/2 - f_{11} + f_{10} + f_{12}$ $f_7 = (-f_1 + f_2 - f_3 + f_4)/2 + f_8 + f_{11} - f_{12}$
7	$f_5 = f_6$ $f_{11} = (f_3 - f_4)/2 - f_{13} + f_{12} + f_{14}$ $f_9 = (f_1 - f_2 - f_3 + f_4)/2 + f_{13} - f_{14} + f_{10}$ $f_7 = (-f_1 + f_2)/2 + f_8 - f_{13} + f_{14}$
8	$f_5 = f_6$ $f_{11} = (f_3 - f_4 + f_1 - f_2)/2 + f_7 - f_8 + f_{12}$ $f_9 = (-f_3 + f_4)/2 - f_7 + f_8 + f_{10}$ $f_{13} = (-f_1 + f_2)/2 - f_7 + f_8 + f_{14}$
9	$f_{13} = f_{14} \quad ; \quad f_7 = f_8$
10	$f_9 = f_{10} \quad ; \quad f_7 = f_8$
11	$f_9 = f_{10} \quad ; \quad f_{11} = f_{12}$
12	$f_{13} = f_{14} \quad ; \quad f_{11} = f_{12}$
13	$f_5 = f_6$ $f_1 = 2(-f_{10} + f_9 + f_{11} - f_{12}) + f_2$ $f_{13} = (f_3 - f_4)/2 - f_{11} + f_{12} + f_{14}$ $f_7 = (-f_3 + f_4)/2 + f_8 - f_9 + f_{10}$

Label (see fig.2)	Conditions
14	$f_5 = f_6$ $f_9 = (f_1 - f_2)/2 - f_{11} + f_{10} + f_{12}$ $f_7 = (-f_1 + f_2)/2 + f_8 - f_{13} + f_{14}$ $f_3 = 2(-f_{12} + f_{11} + f_{13} - f_{14}) + f_4$
15	$f_5 = f_6$ $f_2 = 2(-f_{14} + f_7 + f_{13} - f_8) + f_1$ $f_{11} = (f_3 - f_4)/2 - f_{13} + f_{12} + f_{14}$ $f_9 = (-f_3 + f_4)/2 + f_8 - f_7 + f_{10}$
16	$f_5 = f_6$ $f_{11} = (f_1 - f_2)/2 - f_9 + f_{10} + f_{12}$ $f_{13} = (-f_1 + f_2)/2 - f_7 + f_8 + f_{14}$ $f_4 = 2(-f_{10} + f_7 + f_9 - f_8) + f_3$
17	$f_{10} = f_9$; $f_{13} = f_{14}$
18	$f_7 = f_8$; $f_{12} = f_{11}$
19	$f_9 = f_{10}$; $f_{14} = f_{13}$
20	$f_8 = f_7$; $f_{11} = f_{12}$
21	$f_1 = f_2$; $f_7 = f_8$ $f_{12} = (-f_3 + f_4)/2 + f_{11}$ $f_{13} = (-f_5 + f_6)/2 + f_{14}$ $f_{10} = (f_3 - f_4 + f_5 - f_6)/2 + f_9$
22	$f_3 = f_4$; $f_7 = f_8$ $f_9 = (-f_5 + f_6)/2 + f_{10}$ $f_{14} = (f_1 - f_2 + f_5 - f_6)/2 + f_{13}$ $f_{12} = (-f_1 + f_2)/2 + f_{11}$
23	$f_2 = f_1$; $f_8 = f_7$ $f_{11} = (f_3 - f_4)/2 + f_{12}$ $f_{14} = (f_5 - f_6)/2 + f_{13}$ $f_9 = f_{10} + (-f_3 + f_4 - f_5 + f_6)/2$
24	$f_8 = f_7$; $f_4 = f_3$ $f_{11} = (f_1 - f_2)/2 + f_{12}$ $f_{10} = (f_5 - f_6)/2 + f_9$ $f_{13} = (-f_5 + f_6 - f_1 + f_2)/2 + f_{14}$
25	$f_7 = f_8$; $f_5 = f_6$ $f_{11} = (f_1 - f_2 + f_3 - f_4)/2 + f_{12}$

Label (see fig.2)	Conditions
	$f_9 = (-f_3 + f_4)/2 + f_{10}$ $f_{13} = (-f_1 + f_2)/2 + f_{14}$
26	$f_7 = f_8 ; f_5 = f_6$ $f_{11} = (f_1 - f_2 + f_3 - f_4)/2 + f_{12}$ $f_9 = (-f_3 + f_4)/2 + f_{10}$ $f_{13} = (-f_1 + f_2)/2 + f_{14}$
27	$f_6 = f_5 ; f_8 = f_7$ $f_{10} = (f_3 - f_4)/2 + f_9$ $f_{14} = (f_1 - f_2)/2 + f_{13}$ $f_{12} = (-f_3 + f_4 - f_1 + f_2)/2 + f_{11}$

References

- [1] J. Bico, C. Marzolin, and D. Quéré. Pearl drops. *Europhys. Lett.*, 47:220, 1999.
- [2] D. Öner and T.J. McCarthy. Ultrahydrophobic surfaces. Effects of topography length scales on wettability. *Langmuir*, 16:7777, 2000.
- [3] B. He, N.A. Patankar, and J. Lee. Multiple equilibrium droplet shapes and design criterion for rough hydrophobic surfaces. *Langmuir*, 19:4999, 2003.
- [4] N.A. Patankar. Transition between superhydrophobic states on rough surfaces. *Langmuir*, 20:7097, 2004.
- [5] C. Ishino, K. Okumura, and D. Quéré. Wetting transitions on rough surfaces. *Europhys. Lett.*, 68:419, 2004.
- [6] J. Léopoldès, A. Dupuis, D.G. Bucknall, and J.M. Yeomans. Jetting micron-scale droplets onto chemically heterogeneous surfaces. *Langmuir*, 19:9818, 2003.
- [7] A.J. Briant, A.J. Wagner, and J.M. Yeomans. Lattice Boltzmann simulations of contact line motion. I. Liquid-gas systems. *Phys. Rev. E*, 69:031602, 2004.
- [8] J.W. Cahn. Critical point wetting. *J. Chem. Phys.*, 66:3667, 1977.
- [9] D.M. Anderson, G.B. McFadden, and A.A. Wheeler. Diffuse-interface methods in fluid mechanics. *Annu. Rev. Fluid Mech.*, 30:139, 1998.

- [10] M.R. Swift, E. Orlandini, W.R. Osborn, and J.M. Yeomans. Lattice Boltzmann simulations of liquid-gas and binary fluid systems. *Phys. Rev. E*, 54:5051, 1996.
- [11] A. Dupuis and J.M. Yeomans. Lattice Boltzmann modelling of droplets on chemically heterogeneous surfaces. *Fut. Gen. Comp. Syst.*, 20:993, 2004.
- [12] D. Jacqmin. Contact-line dynamics of a diffuse fluid interface. *J. Fluid Mech.*, 402:57, 2000.
- [13] A. Lafuma and D. Quéré. Superhydrophobic states. *Nature Materials*, 2:457, 2003.